nature communications

Article

https://doi.org/10.1038/s41467-026-77178-9

Photon-driven magnetization switching in Fe_3GeTe_2 enables programmable, multilevel magnetic memory

Received: 20 November 2025

Accepted: 19 August 2026

Published online: 02 September 2026

Check for updates

Wei-Qing Li[1,7], Sheng-Hsiung Hung[2,7], Jia-Xin Li[1], Chung-Chun Lu[1], Po-Liang Chen[1], Ching Kuo[1], Kun-Hung Pan[1], Horng-Tay Jeng[2,3,4] ✉ & Chang-Hua Liu[1,5,6] ✉

The rediscovery of van der Waals magnets has revitalized research into intrinsic two-dimensional magnetism and motivated unconventional strategies, such as electrostatic gating and strain, to switch magnetic states. Photon-driven magnetization switching, however, remains largely unexplored but holds promise for fast, high-density, and energy-efficient spintronic applications. Here, we show that the itinerant van der Waals ferromagnet Fe_3GeTe_2 exhibits tunable magnetism under optical pulsed excitation, with the response governed by photon energy, fluence, and polarization. This is evident from our magneto-optic measurements, which reveal that pulses with 2.3 eV photon energy effectively reduce the coercivity of Fe_3GeTe_2. When coercivity is sufficiently lowered by strong pulse fluence, the magnetic order becomes helicity-dependent, enabling reversible suppression and restoration of the out-of-plane magnetization. Further studies indicate that these phenomena originate from distinct semiconductor-like transitions in Fe_3GeTe_2, through which photons of opposite helicity induce distinct modifications in the electronic structure, thereby altering magnetic anisotropy and the ground state differently via optical doping effect. Building on this understanding, we further demonstrate the potential of Fe_3GeTe_2 for optically controlled nonvolatile memory, capable of multilevel information storage with reversible writing and erasing, as well as spatially defined spin states, offering promise for next-generation spintronics.

Understanding the interplay between photons and spin systems is both of fundamental interest and a central focus of modern spintronics, as optical excitation can tune magnetic anisotropy energy (MAE) and spatially pattern spin structures[1,2]. Beyond these effects, magnetization can also be switched reversibly using light alone, without external magnetic fields or electric currents. This phenomenon, known as all-optical switching (AOS), offers the potential for high-speed, high-density, and energy-efficient magnetic memory[3–5]. So far, AOS has been predominantly demonstrated in rare-earth transition-metal ferrimagnetic alloys, such as GdFeCo and TbCo[5–7], via two main approaches. One involves a single femtosecond laser pulse to drive the electronic system into a highly non-equilibrium state; during subsequent cooling, angular momentum transfer between antiferromagnetically coupled sublattices via conduction electrons

[1]Institute of Photonics Technologies, National Tsing Hua University, Hsinchu, Taiwan, ROC. [2]Department of Physics, National Tsing Hua University, Hsinchu, Taiwan, ROC. [3]Institute of Physics, Academia Sinica, Taipei, Taiwan, ROC. [4]Physics Division, National Center for Theoretical Sciences, Taipei, Taiwan, ROC. [5]Department of Electrical Engineering, National Tsing Hua University, Hsinchu, Taiwan, ROC. [6]College of Semiconductor Research, National Tsing Hua University, Hsinchu, Taiwan, ROC. [7]These authors contributed equally: Wei-Qing Li, Sheng-Hsiung Hung. ✉e-mail: jeng@phys.nthu.edu.tw; chliu@ee.nthu.edu.tw

determines the magnetization orientation, enabling single-shot switching between out-of-plane states ($M\downarrow/M\uparrow$)[8,9]. The other approach employs multi-shot excitation with helicity control, where laser pulses heat the material near its Curie point, allowing left- (σ^-) and right- (σ^+) circularly polarized pulses to direct the magnetization toward opposite out-of-plane orientations (i.e., helicity-dependent AOS). While the exact origins remain debated, the inverse Faraday effect, magnetic circular dichroism, and light-induced angular momentum transfer are considered possible mechanisms[7,10–12]. Beyond metallic systems, helicity-dependent AOS has also been demonstrated in ferromagnetic semiconductors, such as (Ga,Mn)As, but with a non-thermal origin. In this case, near-bandgap circularly polarized excitation generates spin-polarized holes that drive collective Mn spin rotation, causing magnetization reversal[13]. Despite these advances, practical application of AOS in spintronic devices remains challenged by the requirements for precise metal alloy deposition or complex epitaxial growth, complicating device fabrication and integration[4].

In contrast, van der Waals (vdW) magnets are considered a potential alternative due to their layered structure, which allows exfoliation into atomically thin crystals, integration into two-dimensional (2D) heterostructures, and assembly on various substrates without lattice mismatch[14–16]. Their ultrathin nature also renders their magnetic properties susceptible to external stimuli, making it possible to reversibly tune magnetic states via strain and electrostatic gating[17–20]. By comparison, experimental demonstrations of AOS of magnetic states in vdW magnet remains limited, with only a few reports on few-layer CrI_3[21,22]. This material owns layered antiferromagnetism with out-of-plane spin orientation (type-A antiferromagnetic order)[23], and helicity-dependent AOS has been demonstrated based on trilayer CrI_3, showing switching between ↑↓↑ and ↓↑↓ two layered-antiferromagnetic states. This switching is likely driven by spin angular momentum transfer from photoexcited carriers to localized magnetic moments[21]. Helicity-dependent AOS has also been observed in bulk CrI_3/monolayer WSe_2 heterostructures. In such system, pulses trigger thermal demagnetization in CrI_3, and interfacial charge transfer of photoexcited spin-polarized carriers from WSe_2 to CrI_3 governs the net magnetization during the subsequent cooling process[22].

Beyond CrI_3, Fe_3GeTe_2 (FGT) is a noteworthy emerging vdW magnet, known as an itinerant ferromagnet with strong perpendicular magnetic anisotropy and a high Curie temperature (~200 K in its bulk state)[24,25]. Although AOS has not yet been realized in FGT, prior studies have shown that its magnetism can be controlled optically. For example, femtosecond pulse excitation can transiently tune saturation magnetization, coercivity, and Curie temperature via optical-doping-induced changes in the electronic structure[26]. Additionally, circularly polarized CW excitation during zero-field cooling can guide magnetic domain formation, likely mediated by optically injected spin-polarized electrons[27]. Here, we extend these studies and demonstrate helicity-dependent AOS in FGT. Specifically, we show that pulsed excitation involving interband transitions in FGT enables modulation of the coercive field and control of the remanent magnetization. Notably, the remanent magnetization exhibits helicity-dependent, non-volatile switching: upward (downward) out-of-plane magnetization can be fully suppressed by σ^- (σ^+) pulses and restored by reversing the helicity, as confirmed by reflective magnetic circular dichroism (RMCD) measurements and theoretical calculations. Exploiting these features, we further demonstrate the potential of FGT for optically controlled magnetic memory.

Results

Observation of pulsed-laser-induced coercivity reduction and AOS in FGT

We begin the measurements using a 10-layer-thick exfoliated FGT flake (see "Methods" and Supplementary Section 1 for thickness characterization), shown in the optical microscope image in Fig. 1a, with its crystal structure illustrated in Fig. 1b. The sample was mounted in a cryogenic optoelectronic setup (Fig. 1c), cooled to 30 K, and equipped with an electromagnet capable of applying an out-of-plane magnetic field. To probe and manipulate the magnetic properties of FGT, two laser beams were collinearly focused onto the flake. A continuous-wave HeNe laser ($\lambda = 633$ nm) was used for polar RMCD measurements, while a picosecond pulsed laser was used to optically modulate its magnetization (see "Methods"). Figure 1d shows the normalized RMCD loop of FGT without pulsed excitation. It features remanent magnetizations (M_r^+, M_r^-) close to their respective saturation magnetizations ($M_{s,0}^+$, $M_{s,0}^-$), with symmetric coercive fields ($|H_c^+|$ and $|H_c^-|$) of ~250 mT (Fig. 1d). This square-shaped hysteresis loop and large coercivity reflect a single magnetic domain and strong MAE[24,25].

Upon pulsed laser excitation, distinct changes in the magnetic properties of FGT emerge, which can be categorized into two excitation power regimes for analysis. Figure 1e presents RMCD loop measurements recorded while simultaneously illuminating the sample under linearly (π)-polarized pulsed excitation ($\lambda = 540$ nm) with power levels below 250 μW. Each loop is normalized to $M_{s,0}^+$, the positive saturation magnetizations without pulsed perturbation, for comparison. At low powers, the hysteresis loop remains unchanged up to approximately 170 μW (Fig. 1f). Beyond this threshold, the remanent-to-saturation magnetization ratio remains close to unity, while the coercive field ($H_c = (|H_c^+| + |H_c^-|)/2$) decreases sharply to 20 mT with symmetrical reductions the amplitudes of H_c^+ and H_c^-, indicating pulsed excitation could reduce MAE of FGT. We further observe that the pulse-induced variations in coercivity within the examined power range (<250 μW) are polarization-independent (Supplementary Section 2) but strongly dependent on the photon energy of pulses. The most pronounced response occurs at $\lambda = 540$ nm (Fig. 1g), corresponding to a photon energy of ~2.3 eV that coincides with an electronic transition energy in FGT, as revealed by recent microthermoreflectance and differential reflectance measurements and supported by density functional theory (DFT) calculations[28,29]. This spectral correspondence implies that photocarrier generation in FGT could play a key role in modulating its magnetic properties.

Next, we present RMCD measurements under pulsed ($\lambda = 540$ nm) excitation powers exceeding 250 μW, revealing that in this high-power regime, the polarization of the pulses appears to influence the loop characteristics. This is illustrated in Fig. 2a, b, which show RMCD loops measured at 270 and 300 μW, respectively. Under σ^+-, π-, and σ^--polarized pulsed excitation, the loops exhibit distinct variations within the ±25 mT field range, and variations become more pronounced at higher powers, as further illustrated in the zoomed-in views of this range (Fig. 2c, d). Importantly, these detailed views clearly demonstrate that the remanent magnetization decreases in a polarization-sensitive manner. For π-polarized excitation, both M_r^+ and M_r^- show modest and symmetric reductions. In contrast, σ^--polarized (σ^+-polarized) light markedly suppresses M_r^+ (M_r^-) but leaves M_r^- (M_r^+) largely unchanged, exhibiting a pronounced asymmetry. The full polarization-dependent evolution of M_r^+ and M_r^- as a function of excitation powers are shown in Fig. 2e, f. These trends clearly indicate that once the coercivity is sufficiently reduced by intense pulsed excitation, photon helicity could function as a control parameter for manipulating the magnetic order in FGT.

In addition to the helicity-dependent suppression, we further demonstrate that the suppressed remanent magnetization can be reversibly restored to its original out-of-plane configuration by pulses of opposite helicity, and that both the suppression and recovery behaviors are nonvolatile. Figure 3a (lower panel) presents the temporal evolution of the RMCD signal from FGT at zero magnetic field, in response to the helicity-varying pulse sequence shown in the upper panel. Prior to pulse excitation, the remanent magnetization of FGT was initialized in the fully $M\uparrow$ state (i.e., $M_r^+/M_{s,0}^+$~1) by sweeping the magnetic field from 0.3 T to 0 T. Upon exposure to 300 μW σ^--

https://doi.org/10.1038/s41467-026-77178-9

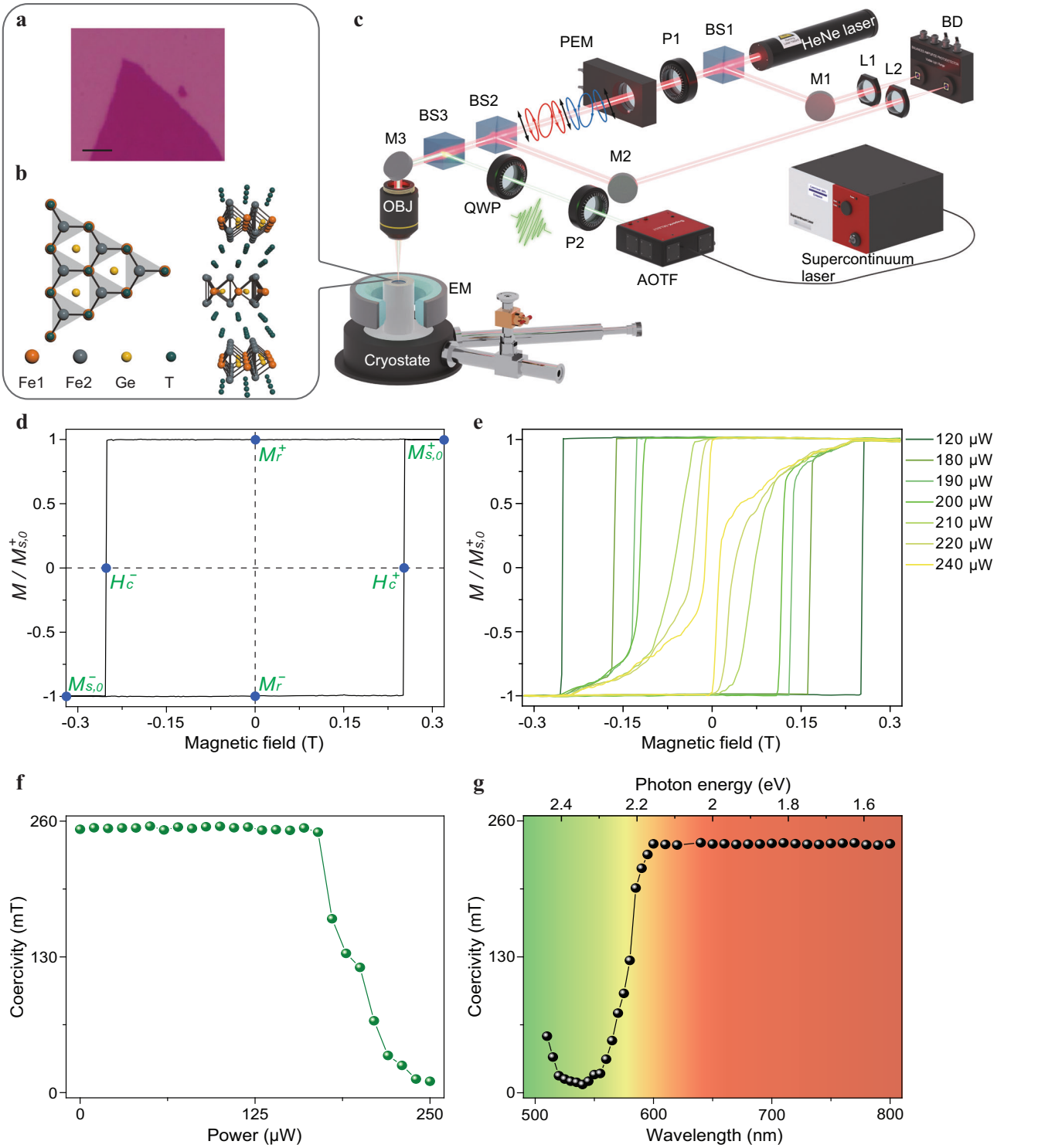

Fig. 1 | Experimental setup and observation of coercivity reduction in FGT under pulsed excitation. a Optical microscope image of a 10-layer-thick FGT flake. Scalar bar: 3 μm. **b** Schematic crystal structure of FGT shown from the top view (left) and side view (right). **c** Schematic illustration of the experimental setup for characterizing magnetic properties of FGT. BD, balanced detector; L: lens; M: mirror; BS: beam splitter; P: polarizer; PEM: photo-elastic modulator; AOTF: acousto-optic tunable filter; QWP: quarter waveplate; OBJ: objective lens; EM: electromagnet. **d** Polar RMCD magnetic hysteresis loops of FGT measured without pulsed excitation, normalized with respect to its positive saturation magnetization, $M_{s,0}^+$. The blue dots mark the positive and negative coercive fields (H_c^+ and H_c^-), remanent magnetizations (M_r^+ and M_r^-), and saturation magnetizations ($M_{s,0}^+$ and $M_{s,0}^-$). **e** Polar RMCD magnetic hysteresis loops of FGT measured under π-polarized pulsed excitation at different powers, normalized to $M_{s,0}^+$, the upward saturation magnetization of FGT without pulsed perturbation. **f** Extracted coercive field of FGT as a function of π-polarized pulsed excitation powers. **g** Measured coercive field of FGT under π-polarized pulsed excitation at different wavelengths, with power fixed at 260 μW.

https://doi.org/10.1038/s41467-026-77178-9

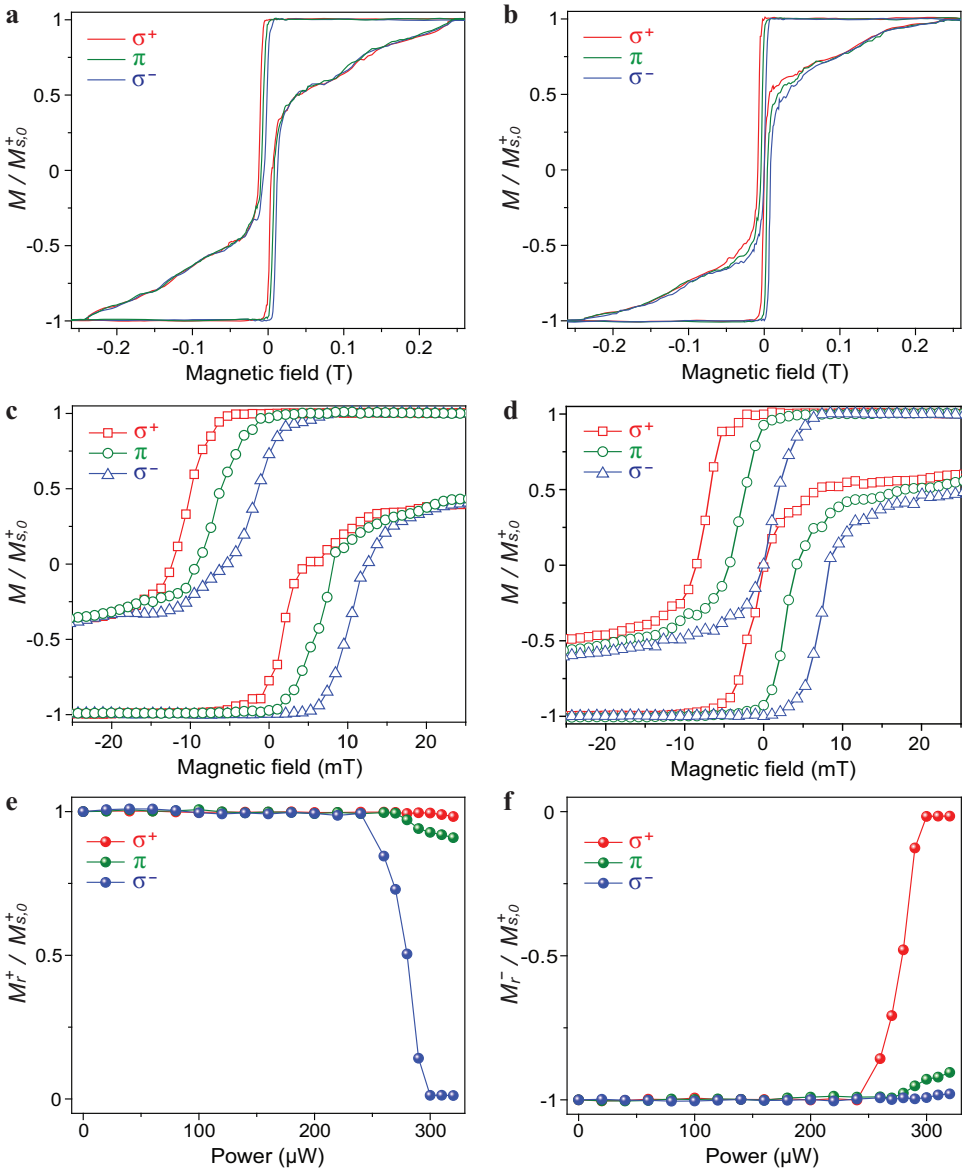

Fig. 2 | Observation of polarization-dependent change in remanent magnetization of FGT. a Normalized polar RMCD hysteresis loops of FGT under σ^+ (red), π (green), and σ^- (blue) pulsed excitation at a fixed power of 270 μW. **b** Normalized polar RMCD hysteresis loops of FGT under σ^+ (red), π (green), and σ^- (blue) pulsed excitation at a fixed power of 300 μW. **c** Zoom-in view of the RMCD hysteresis loops in (**a**). **d** Zoom-in view of the RMCD hysteresis loops in (**b**). The loops in (**a**–**d**) are normalized to $M^+_{s,0}$, the upward saturation magnetization of FGT without pulsed perturbation. Plot of the power-dependent change in **e** $M^+_r/M^+_{s,0}$, and **f** $M^-_r/M^+_{s,0}$ under σ^+ (red), π (green), and σ^- (blue) polarized pulsed excitation.

polarized pulsed excitation, the $M\uparrow$ out-of-plane magnetic order is fully suppressed and remains stable even after the excitation is turned off (also see Supplementary Section 3 for a retention time exceeding 10^4 s), confirming the non-volatile nature of this helicity-driven switching. Remarkably, subsequent application of 300 μW σ^+-polarized pulses restores the remanent magnetization non-volatilely to the original fully $M\uparrow$ state, without the need for an external magnetic field (also see Supplementary Section 3 for endurance exceeding 10^3 switching cycles). A similar behavior is observed for FGT initially in the fully $M\downarrow$ state (i.e., $M^-_r/M^+_{s,0}\sim-1$), but with the opposite helicity response. In this case, 300 μW σ^+-polarized pulses suppress the remanent magnetization, while 300 μW σ^--polarized pulses restore it, as shown in Fig. 3b. These results provide clear evidence of helicity-dependent, nonvolatile AOS in FGT magnetization.

Beyond the binary AOS between the fully out-of-plane and suppressed states, we note that careful tuning of the pulsed excitation power between 250 and 300 μW results in intermediate RMCD values, spanning $0 \le M^+_r/M^+_{s,0} \le 1$ (Fig. 2e) or $-1 \le M^-_r/M^+_{s,0} \le 0$ (Fig. 2f), offering the possibility of multistate data storage. We demonstrate this for FGT initially at full $M\downarrow$ remanence (see Supplementary Section 4 for multistate control with FGT initially at full $M\uparrow$ remanence). In Fig. 3c, the upper panel displays a sequence of σ^+-polarized pulses with powers of 260, 270, 280, and 285 μW, each applied for 2 s with 118-s dark intervals. The corresponding RMCD signal in the lower panel reveals stepwise reductions in amplitude of $M^-_r/M^+_{s,0}$ by approximately 15%, 25%, 50%, and 70%. Notably, each intermediate state remains stable after the pulse excitation is switched off, confirming the non-volatile nature of these multilevel magnetization states. Moreover, the original fully $M\downarrow$ state can be restored with a 300 μW σ^--polarized pulsed excitation, demonstrating FGT as a platform for light-programmable multilevel memory with potential for high-capacity data storage.

https://doi.org/10.1038/s41467-026-77178-9

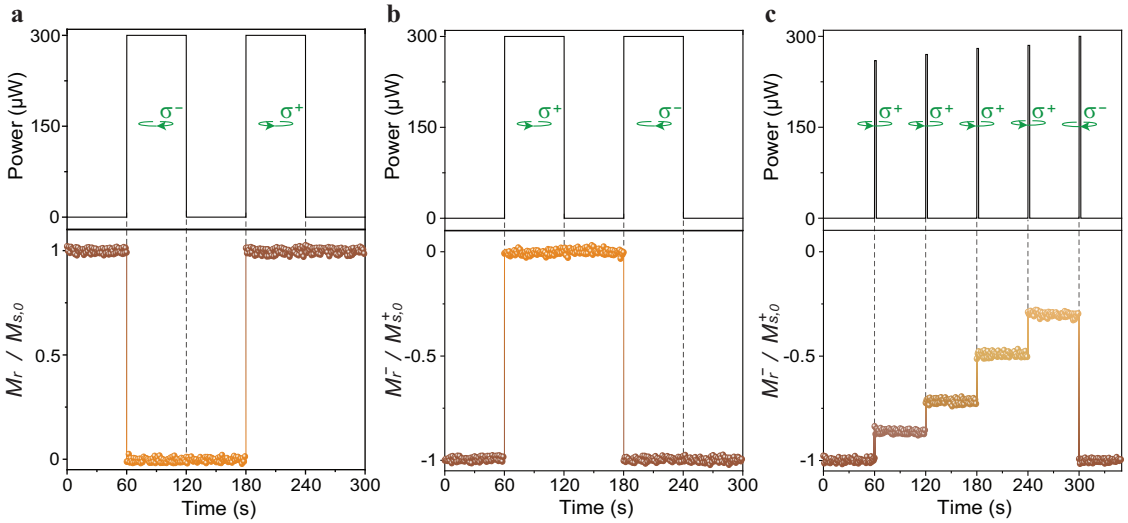

Fig. 3 | Demonstration of helicity-dependent AOS of remanent magnetization in FGT. a Temporal response of $M_r^+/M_{s,0}^+$ in FGT (lower panel), with the remanent magnetization initially set in the fully $M\uparrow$ state, under sequential σ^- and σ^+ pulsed illumination (top panel). The results show that the upward remanent magnetization, $M\uparrow$, can be suppressed by σ^- pulses and restored by σ^+ pulses in a nonvolatile manner. **b** Temporal response of $M_r^-/M_{s,0}^+$ in FGT (lower panel), with the remanent magnetization initially set in the fully $M\downarrow$ state, under sequential σ^+ and σ^- pulsed illumination (top panel). The results show that the downward remanent magnetization, $M\downarrow$, can be suppressed by σ^+ pulses and restored by σ^- pulses in a nonvolatile manner. **c** Temporal response of $M_r^-/M_{s,0}^+$ in FGT (lower panel), with the remanent magnetization initially set in the fully $M\downarrow$ state, under sequential σ^+ pulsed illumination at 260, 270, 280, and 285 μW, followed by σ^- pulses at 300 μW (top panel). Each illumination period lasted 2 s. The corresponding multilevel magnetic states remain stable after each pulsed excitation sequence, confirming their nonvolatile nature. All measurements in (**a**–**c**) were performed without an external magnetic field, using a pulsed laser with a wavelength of 540 nm.

Discussion and theoretical analysis of FGT under pulsed excitation

After presenting the phenomenological observations, we now discuss how the helicity-dependent AOS behavior in FGT differs from that in conventional metallic magnetic alloys. In these alloys, AOS is primarily associated with thermal effects induced by pulsed excitation that raise the system close to its Curie temperature, thereby making the magnetization susceptible to photon helicity[1,2,7,10–12]. Because their absorption spectrum is relatively flat across the commonly used pulsed-laser wavelength range (visible-near-IR), this process shows weak photon-energy dependence. FGT, on the other hand, exhibits a markedly different response, with its magnetism modulated as pulse photon energy corresponds to an electronic transition. Although this transition may induce heating, our simulations indicate that under 300 μW pulsed excitation, the peak transient temperature of FGT reaches only ~52 K (Supplementary Section 5), well below its Curie temperature (~200 K). Moreover, our power-dependent hysteresis measurements (Figs. 1f and 2e, f) reveal a two-stage response: an initial decrease in coercive field, followed by a helicity-dependent suppression of remanent magnetization as excitation power increases. This behavior differs from temperature-dependent RMCD results for FGT reported in the literature[24,30] and observed in our measurements (Supplementary Section 6), where both coercivity and remanent magnetization decline as temperature rises, pointing to a nonthermal origin under pulse excitation. Another key distinction is that FGT exhibits helicity-driven transitions between fully saturated and suppressed out-of-plane magnetization, the latter likely corresponding to in-plane or type-A antiferromagnetic order. This contrasts with the discrete $M\uparrow/M\downarrow$ switching observed in typical metallic alloys[2–4], implying that photon helicity plays a fundamentally different role in FGT.

To clarify the distinct AOS behavior in FGT, we perform DFT calculations (see "Methods") to understand the impact of pulsed excitation and how photon helicity alters the magnetic ordering of FGT. Our calculations reveal that pulsed excitation induces a high density of excited holes near the Fermi level (i.e., optical doping effect; see Supplementary Section 7 for further evidence)[26–28]. This process depopulates electron pockets near the Fermi level at the K and H points, primarily from orbitals with magnetic quantum number $m = \pm 2$ (Supplementary Section 8), and such depopulation reduces the MAE of FGT[31]. Additionally, the extent of depopulation, and hence MAE reduction, depends on the polarization of the pulses (Fig. 4a). This dependence arises because in the remanent $M\uparrow$ state, σ^-, σ^+, and π polarized pulses selectively excite minority spin-down, majority spin-up, and holes of both spins, respectively, producing distinct modifications to the electronic structure that can even lead to distinct magnetic ground states (Fig. 4a). Specifically, as σ⁻-induced doping exceeds 0.7 hole per formula unit (f.u.), the ground state would transit from out-of-plane ferromagnetic order (Fig. 4a, b) into in-plane ferromagnetic order (Fig. 4a, c), a consequence of the complete depopulation of the electron pockets. In contrast, the same level of hole doping, but induced by σ^+- or π-polarized excitation, only partially depletes the electron pockets, thereby preserving the out-of-plane ground state despite a substantial MAE reduction (Fig. 4a, d, also see Supplementary Section 8 for details on the changes in electronic structure and Section 9 for ground-state calculations). Thus, with FGT prepared in the remanent $M\uparrow$ state prior to pulse excitation, it can be driven into an in-plane ferromagnetic configuration under σ^- excitation and then reversibly returned to the out-of-plane configuration with σ^+ excitation (Fig. 4b–d), establishing the theoretical basis for helicity-dependent AOS in FGT.

Having established that pulse helicity governs the magnetic ground state during transient excitation, we next discuss why the pulse-induced in-plane state persists even after pulse termination, rather than recovering its out-of-plane ground state. We attribute this nonvolatile behavior to two possible intertwined mechanisms. The first is associated with the contrast between illuminated and non-illuminated regions, which induces distinct magnetic configurations and gives rise to domain walls at their boundaries. These domain walls persist after pulse excitation due to domain-wall pinning, as observed in conventional ferromagnetic thin films[32–35]. The second involves phonon modes activated by pulsed excitation, which can persist beyond the pulse and modify the magnetic anisotropy energy[36]. Our DFT calculations analyze a broad set of pulse-activated phonon modes across the Brillouin zone and find that those at the K and M points

https://doi.org/10.1038/s41467-026-77178-9

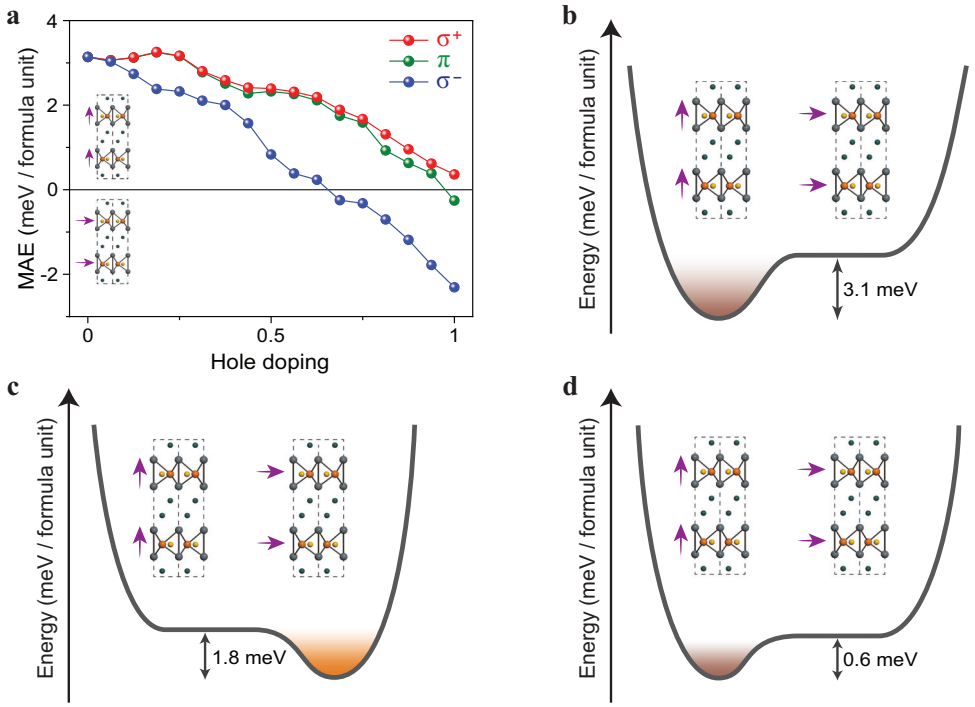

Fig. 4 | DFT calculations of pulsed-excitation-induced changes in MAE and magnetic ground state of FGT. a Calculated changes in the MAE of FGT, defined as the energy difference between in-plane and out-of-plane magnetization, with increasing hole doping induced by σ^+ (red), π (green), and σ^- (blue) polarized pulsed excitation, respectively. Calculated energy landscape of the two lowest-energy magnetic states of **b** FGT with remanent magnetization set in the fully $M\uparrow$ state without pulsed perturbation; **c** FGT, initially in the fully $M\uparrow$ state, under spin-down one-hole doping per f.u. induced by σ^- pulsed excitation, resulting in a transition to in-plane ferromagnetic ordering as the ground state; and **d** FGT, initially in the fully $M\uparrow$ state, under spin-up one-hole doping per f.u. induced by σ^+ pulsed excitation, leaving the out-of-plane ferromagnetic ground state unchanged despite a reduced energy difference with the in-plane configuration. Orange and brown shading indicate stabilization of the in-plane and out-of-plane ferromagnetic states, respectively.

produce significant negative MAE, rendering the in-plane configuration metastable. This allows FGT initially in the $M\uparrow$ state to be driven into the in-plane state during σ^- pulsed excitation and to remain in the in-plane state after the pulse (see Supplementary Section 10 for further details).

Pulsed excitation on FGT flakes of varying thickness

Following this, we extend our investigation to FGT flakes of varying thickness. We find that their RMCD loops consistently show a marked reduction in coercive field, followed by helicity-dependent suppression of M_r^+ and M_r^- with increasing pulsed excitation power. However, notable variations in the remanent response are observed, as shown in Fig. 5a, which presents normalized $M_r^+/M_{s,0}^+$ versus σ^--excitation power for representative flake thicknesses. First, thicker FGT requires higher excitation power to initiate the reduction in remanent magnetization. This behavior could arise from the strong interlayer exchange interactions within FGT, which require more photons in thicker flakes to collectively reorient their magnetization away from the out-of-plane direction. Second, although all flakes exhibit a reduction in out-of-plane remanent magnetization under sufficient pulsed excitation power, complete suppression of $M_r^+/M_{s,0}^+$ occurs only in flakes thinner than 12 layers, irrespective of layer parity (Fig. 5b). This rules out type-A vdW antiferromagnetic ordering as the ground state, since such ordering would yield a nonzero out-of-plane moment in odd-layer flakes. Instead, this result indicates that the entire flake adopts an in-plane magnetization ground state, consistent with our first-principles calculations. For flakes thicker than 12 layers, $M_r^+/M_{s,0}^+$ cannot be fully suppressed even under intense 400 μW excitation, and the residual out-of-plane magnetization increases with thickness (Fig. 5b). This suggests that the applied pulse power primarily suppresses the out-of-plane magnetization in the top ~12 layers, with diminished effect in deeper regions likely due to limited penetration depth. In contrast, the RMCD probe beam uses photon energy detuned from the electronic transition of FGT, enabling deeper penetration and detection of out-of-plane magnetization in the lower, less pulse-affected layers, as schematically illustrated in Fig. 5c–e. Accordingly, the $M_r^+/M_{s,0}^+$ ratio can be estimated as the fraction of less-affected layers, $(N-12)$, over the total number of layers, N (Fig. 5b, red line). We note that this simple approximation aligns well with the experimental trend.

Demonstration of optically controlled magnetic memory

Building on these findings, we finally explore the potential of FGT for optically controlled memory applications using another flake shown in Fig. 6a. The first demonstrated memory scheme leverages pulsed laser-induced coercivity reduction to achieve magnetization switching, either from $M\downarrow$ to $M\uparrow$ or vice versa, analogous to prior approaches but with coercivity reduction arising from the magnetoelectric effect in FGT[37–39]. For $M\downarrow$ to $M\uparrow$ switching (see Supplementary Section 11 for $M\uparrow$ to $M\downarrow$ switching), the FGT was first initialized in the $M\downarrow$ state (green circle, Fig. 6b) by sweeping the magnetic field from −0.3 to 0.15 T and holding it constant at 0.15 T throughout the experiment. Illumination with a 200 μW pulsed laser then causes the coercivity to drop abruptly below 0.15 T, allowing the applied magnetic field to reverse the magnetization to the $M\uparrow$ state (Fig. 6b). This switching is confirmed by RMCD measurements tracking out-of-plane magnetization as the pulse power increases from 0 to 400 μW (Fig. 6c, black squares), and notably, the magnetization remains in the $M\uparrow$ state after the pulse is turned off, confirming its nonvolatile behavior (Fig. 6c, red dots).

The second memory scheme leverages the helicity-dependent AOS of FGT remanent states. This is demonstrated using a thin FGT flake with its remanent magnetization initially set to the fully $M\downarrow$ state, as shown in the RMCD image in Fig. 6d. The $M\downarrow$ state is prepared by

https://doi.org/10.1038/s41467-026-77178-9

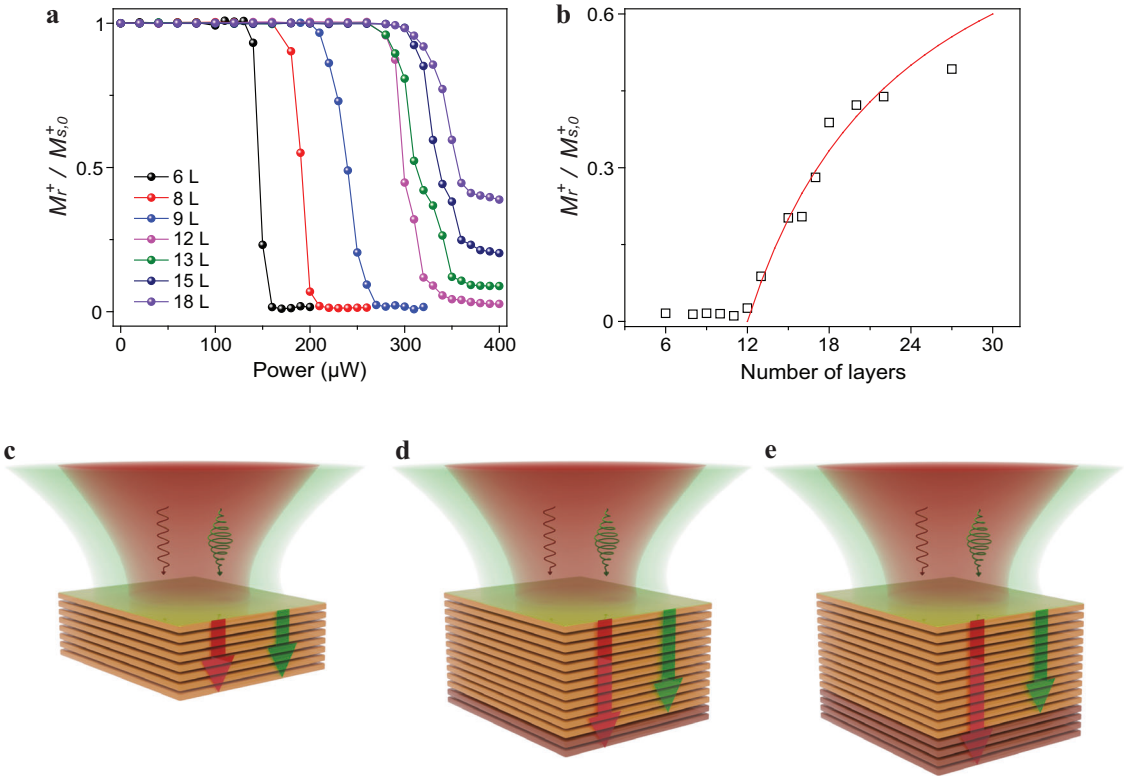

Fig. 5 | Power-dependent change in remanent magnetization of FGT for various thicknesses. a Evolution of $M_r^+/M_{s,0}^+$ in FGT flakes with varying thickness under σ^- pulsed excitation ($\lambda = 540$ nm) as the pulse power was increased from 0 to 400 μW. The remanent magnetization of all flakes was set in the fully $M\uparrow$ state prior to the power-dependent measurements, and for each thickness, the measured positive remanent magnetization (M_r^+) is normalized to the corresponding flake's saturation magnetization ($M_{s,0}^+$). Each data point is obtained by illuminating the FGT with σ^- pulses lasting 2 s; once the pulses ended, M_r^+ was measured using a CW probe beam ($\lambda = 633$ nm). 6 L denotes six layers, with the same notation applied to other thicknesses. **b** Measured $M_r^+/M_{s,0}^+$ values (hollow squares) for FGT flakes of different thicknesses. Each data point was obtained by illuminating the FGT with 400 μW σ^- pulses lasting 2 s; once the pulses ended, M_r^+ was measured using a CW probe beam ($\lambda = 633$ nm). The red line depicts the function $(N - 12)/N$, where N is the total number of layers, describing the increase in $M_r^+/M_{s,0}^+$ for flakes thicker than 12 layers. Schematic illustrations of magnetic ordering in **c** 8-, **d** 14-, and **e** 16-layer FGT flakes under 400 μW σ^- pulsed excitation (green beam), with polar RMCD probed by a CW HeNe laser (red beam). Red and green arrows indicate the penetration depths of the HeNe and pulsed beams, respectively. Each square block represents one FGT layer, with orange and brown blocks indicating in-plane and out-of-plane ferromagnetic ordering, respectively.

sweeping the magnetic field from −0.3 to 0 T and holding it there throughout the experiment. A σ^+-polarized pulsed laser with powers of 310, 280, and 260 μW is then sequentially applied to three distinct locations, locally modifying the magnetic state. The resulting RMCD map (Fig. 6e), acquired after the pulse excitation is switched off, exhibits well-defined spots with different degrees of $M\downarrow$ suppression, as higher pulse powers suppress the out-of-plane magnetization in deeper layers. Notably, these modified regions can be restored to the initial $M\downarrow$ state by scanning them with a σ^--polarized pulsed laser (310 μW), demonstrating reversible switching, as confirmed by the RMCD map acquired after completion of the σ^--polarized pulse scan (Fig. 6f). Such control enables spatially patterned spin alignment for information encoding, which, combined with magnetic-field-free switching for information resetting, offers a route to compact spintronic systems. In conclusion, we experimentally demonstrate that pulsed excitation of electronic transitions in FGT enables control over coercivity and, through helicity dependence, reversible suppression and restoration of the out-of-plane magnetization, with theoretical calculations suggesting that the suppressed state corresponds to an in-plane-favored magnetic configuration. These findings provide new insights into light–magnetism interactions in layered systems and lay the groundwork for exploring similar phenomena in other Fe-based layered magnets exhibiting near-room-temperature ferromagnetism, such as Fe_5GeTe_2, Fe_3GaTe_2, and as well as materials-engineered Fe_3GeTe_2[20,40–45]. Additionally, the observed switching is correlated with a photoexcitation-induced modification of the electronic structure. This process occurs on a sub-picosecond timescale, suggesting that ultrafast optical control can be achieved using femtosecond excitation. However, reducing the pulse duration from the picosecond to femtosecond regime leads to a higher transient electron temperature, potentially introducing additional thermal demagnetization effects that may influence the switching and merit further investigation. In this context, ultrafast time-resolved techniques combined with advanced nanoscale probes could further resolve the evolution of switching pathways and spin textures, as well as the role of disorder-related effects, in greater detail[46–48]. From a technological perspective, our work demonstrates proof-of-concept FGT-based memory devices with optical control and anticipate that this approach can drive progress in areas beyond conventional magnetic thin-film systems. For example, recent studies have integrated FGT with other 2D materials to form vdW heterostructures for spin injector, valleytronics, and magnetic tunneling junctions applications[49–52]. The ability to optically modulate the magnetism of FGT thus offers a practical route for dynamically tuning device electronic properties and functionalities. Moreover, these vdW heterostructures can be readily integrated with diverse on-chip photonics[53,54], collectively opening new avenues for optically controlled reconfigurable logic and information processing.

Methods

Sample preparation

FGT flakes were prepared by mechanical exfoliation onto 285 nm SiO_2/Si substrates. All exfoliation and procedures were performed in a

https://doi.org/10.1038/s41467-026-77178-9

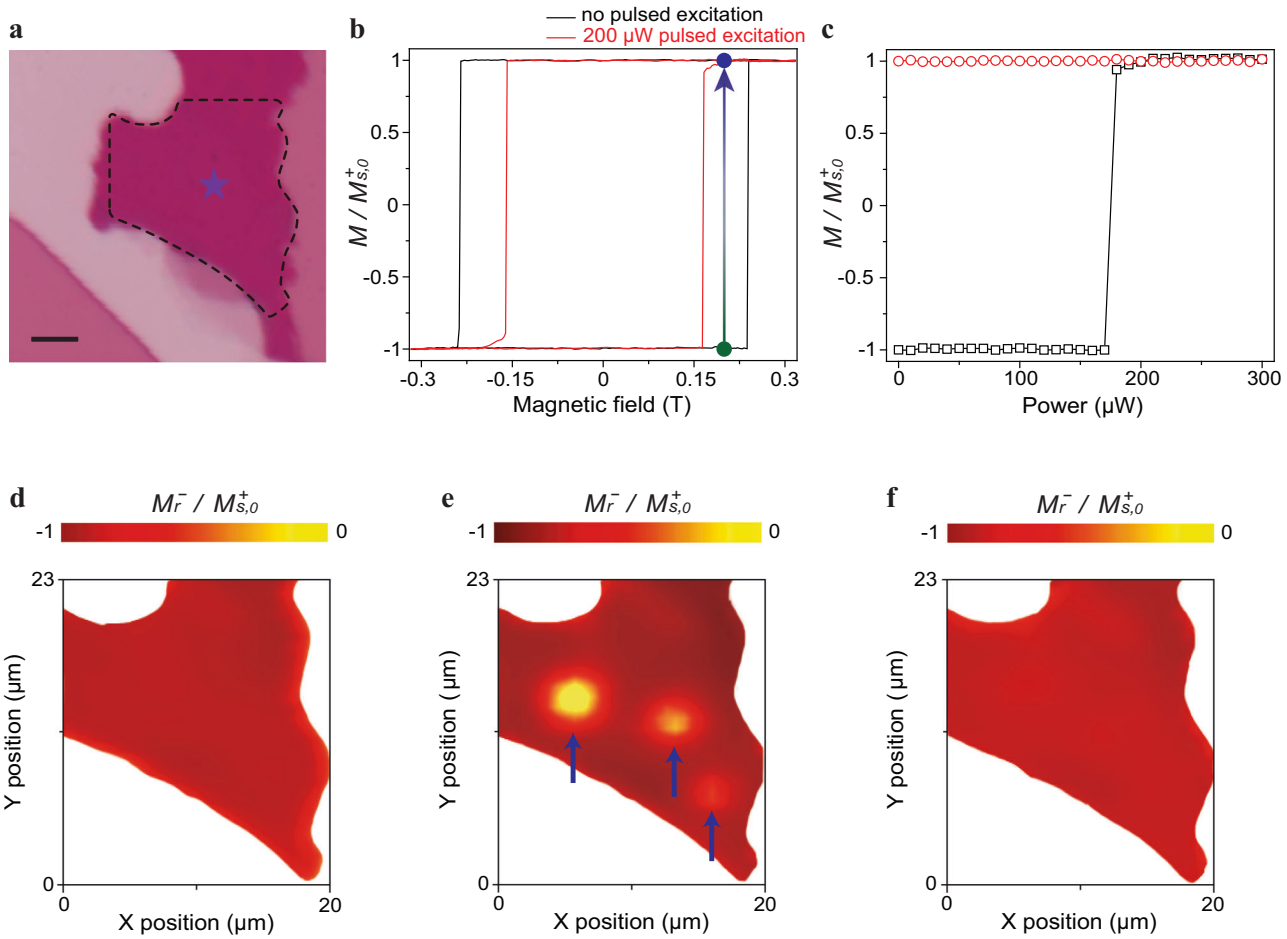

Fig. 6 | Demonstration of optically controlled memory based on FGT. a Optical microscope image of the FGT flake used to demonstrate optically controlled memory concepts. Scalar bar: 5 μm. The purple star indicates the location where the hysteresis loops in (**b**) were measured, and the region outlined by the black dashed line marks the area used for the RMCD maps in (**d**–**f**). **b** Polar RMCD magnetic hysteresis loops of FGT measured without (black) and with (red) π-polarized pulsed excitation. The loops are normalized to $M^{+}_{s,0}$, the upward saturation magnetization of FGT without pulsed perturbation. With the magnetic field fixed at 0.15 T, FGT initially in the fully $M\downarrow$ state (green point) switches to the fully $M\uparrow$ state (blue point) once pulsed excitation lowers the coercivity below the applied magnetic field. **c** Measured $M/M^{+}_{s,0}$ of FGT, initialized at the green-point state in (**b**), under a pulsed excitation power sweep from 0 to 300 μW (black squares) and back from 300 to 0 μW (red circles), with the applied magnetic field fixed at 0.15 T throughout the measurement. At each power step, σ^{-} pulses lasting 2 s were applied, and M was then measured using a CW probe beam ($\lambda = 633$ nm). Spatial RMCD map of FGT at zero magnetic field, measured after **d** sweeping the magnetic field from −0.3 to 0 T, leaving remanent magnetization in the fully $M\downarrow$ state; **e** illuminating the flake in (**d**) with σ^{+} pulses at three positions (left to right: 310, 280, and 260 μW), as indicated by arrows; and **f** raster scanning the flake in (**e**) with σ^{-} pulses (310 μW). The wavelength of the pulsed laser is 540 nm for all optically controlled memory demonstrations.

nitrogen-filled glove box, with oxygen and moisture levels maintained below 0.5 ppm to minimize oxidation. The thicknesses of flakes were initially identified based on optical contrast and subsequently confirmed by AFM. The selected samples were then loaded into a cryostat for magnetic characterization using the RMCD technique. We note the thinnest FGT samples exfoliated on SiO_2/Si substrates are ~6 layers thick. Although thinner flakes can be obtained on exfoliating on gold substrates, we find pulsed excitation in these samples leads to only a negligible reduction in coercivity (see Supplementary Section 12), likely due to electronic hybridization between FGT and gold, which modifies its photon interactions[55].

Optoelectronic measurements

Exfoliated FGT flakes were mounted on the cold finger of a closed-cycle helium cryostat, where the temperature was maintained at 30 K for all measurements unless otherwise noted, and an electromagnet was used to apply an out-of-plane magnetic field. To simultaneously manipulate and probe the magnetic properties of FGT, two laser beams were collinearly focused onto a 1.5 μm spot on the flake using an objective lens. Magnetic manipulation was carried out using pulsed excitation generated by a supercontinuum white light laser (pulse duration ~20 ps, repetition rate 78 MHz) coupled with an acousto-optic tunable filter (AOTF) for wavelength selection. The pulsed beam output from the AOTF then passed through a polarizer and a quarter-wave plate to control its polarization state before being focused onto the FGT. The time-averaged pulse power was kept below 400 μW for all experiments to prevent photodamage to FGT magnetization. The magnetization properties of FGT were probed via RMCD using a linearly polarized HeNe laser beam ($\lambda = 633$ nm) modulated at 50.1 kHz between right- and left-circular polarization by a photoelastic modulator. This modulated light, with a power of 10 μW, was focused normally onto the FGT flake through the objective lens. The reflected beam then returned through the same lens and was subsequently collected by a balanced amplified photodetector to measure the differential reflectivity between the two circular polarization states[24,49]. The detector output was measured using a lock-in amplifier referenced to the PEM modulation frequency (50.1 kHz) to extract the RMCD signal. To improve the signal-to-noise ratio, a power-stabilized HeNe

laser was used together with signal averaging, and hysteresis loops were acquired over repeated cycles to ensure reproducibility.

First-principles calculations

All first-principles calculations in this study were performed using the Vienna Ab initio Simulation Package (VASP)[56–58] based on density functional theory (DFT). The exchange-correlation functional employed was the generalized gradient approximation of the Perdew–Burke–Ernzerhof (GGA-PBE) type[59]. The cutoff energy was set to 400 eV. The $12 \times 12 \times 6$ and $24 \times 24 \times 12$ k-meshes sample the Brillouin zone for ground-state electronic structure calculations and for the MAE calculations using the force theorem[60], respectively. The DFT-D3 method of Grimme with a zero-damping function was considered to correct the vdW interaction[61]. The convergence tolerances were set to 10^{-6} eV for the total energy and 0.01 eV/ Å for the force on each atom. The helicity-dependent hole doping is modeled by simultaneously reducing the number of total electron and constraining the total magnetic moment with respect to the undoped ferromagnetic bulk FGT. Specifically, to simulate σ^--induced spin-down hole doping of one hole per formula unit (f.u.), we remove one electron from the system and increase the total magnetic moment by $1\,\mu_B$, thereby enforcing that the hole resides in the minority spin channel. For σ^+-induced spin-up hole doping, we remove one electron from the system and instead decrease the total magnetic moment by $1\,\mu_B$. For linearly polarized (π) excitation, one electron is removed without applying spin constraint; the total magnetic moment is determined self-consistently. Under these conditions, each system is calculated self-consistently, yielding the spin-selected doping-dependent electronic structure and MAE presented in the manuscript.

Data availability

The data generated in this study have been deposited in the Figshare database under accession code https://doi.org/10.6084/m9.figshare.32064732.

References

1. Kirilyuk, A., Kimel, A. V. & Rasing, T. Ultrafast optical manipulation of magnetic order. *Rev. Mod. Phys.* **82**, 2731–2784 (2010).
2. Kalashnikova, A. M., Kimel, A. V. & Pisarev, R. V. Ultrafast opto-magnetism. *Phys. Uspekhi* **58**, 969–980 (2015).
3. Kimel, A. V. & Li, M. Writing magnetic memory with ultrashort light pulses. *Nat. Rev. Mater.* **4**, 189–200 (2019).
4. Dikshit, S. N. et al. Optically assisted ultrafast spintronics: a review. *Phys. Rep. Rev. Sect. Phys. Lett.* **1140**, 1–46 (2025).
5. Lambert, C. H. et al. All-optical control of ferromagnetic thin films and nanostructures. *Science* **345**, 1337–1340 (2014).
6. Stanciu, C. D. et al. All-optical magnetic recording with circularly polarized light. *Phys. Rev. Lett.* **99**, 047601 (2007).
7. Mangin, S. et al. Engineered materials for all-optical helicity-dependent magnetic switching. *Nat. Mater.* **13**, 286–292 (2014).
8. Radu, I. et al. Transient ferromagnetic-like state mediating ultrafast reversal of antiferromagnetically coupled spins. *Nature* **472**, 205–208 (2011).
9. Graves, C. E. et al. Nanoscale spin reversal by non-local angular momentum transfer following ultrafast laser excitation in ferrimagnetic GdFeCo. *Nat. Mater.* **12**, 293–298 (2013).
10. van der Ziel, J. P., Pershan, P. S. & Malmstrom, L. D. Optically-induced magnetization resulting from the inverse Faraday effect. *Phys. Rev. Lett.* **15**, 190–193 (1965).
11. Gorchon, J., Yang, Y. & Bokor, J. Model for multishot all-thermal all-optical switching in ferromagnets. *Phys. Rev. B* **94**, 020409 (2016).
12. Stanciu, C. D. et al. Ultrafast spin dynamics across compensation points in ferrimagnetic GdFeCo: the role of angular momentum compensation. *Phys. Rev. B* **73**, 220402 (2006).
13. Oiwa, A., Mitsumori, Y., Moriya, R., Słupinski, T. & Munekata, H. Effect of optical spin injection on ferromagnetically coupled Mn spins in the III-V magnetic alloy semiconductor (Ga,Mn)As. *Phys. Rev. Lett.* **88**, 137202 (2002).
14. Gibertini, M., Koperski, M., Morpurgo, A. F. & Novoselov, K. S. Magnetic 2D materials and heterostructures. *Nat. Nanotechnol.* **14**, 408–419 (2019).
15. Jariwala, D., Marks, T. J. & Hersam, M. C. Mixed-dimensional van der Waals heterostructures. *Nat. Mater.* **16**, 170–181 (2017).
16. Gong, C. & Zhang, X. Two-dimensional magnetic crystals and emergent heterostructure devices. *Science* **363**, eaav4450 (2019).
17. Jiang, X. et al. Recent progress on 2D magnets: fundamental mechanism, structural design and modification. *Appl. Phys. Rev.* **8**, 031305 (2021).
18. Cenker, J. et al. Reversible strain-induced magnetic phase transition in a van der Waals magnet. *Nat. Nanotechnol.* **17**, 256–261 (2022).
19. Jiang, S. W., Shan, J. & Mak, K. F. Electric-field switching of two-dimensional van der Waals magnets. *Nat. Mater.* **17**, 406–410 (2018).
20. Park, J.-G. et al. 2D van der Waals magnets: from fundamental physics to applications. *Rev. Mod. Phys.* **98**, 025003 (2026).
21. Zhang, P. Y. et al. All-optical switching of magnetization in atomically thin CrI_3. *Nat. Mater.* **21**, 1373–1378 (2022).
22. Dabrowski, M. et al. All-optical control of spin in a 2D van der Waals magnet. *Nat. Commun.* **13**, 5976 (2022).
23. Huang, B. et al. Layer-dependent ferromagnetism in a van der Waals crystal down to the monolayer limit. *Nature* **546**, 270–273 (2017).
24. Fei, Z. Y. et al. Two-dimensional itinerant ferromagnetism in atomically thin Fe_3GeTe_2. *Nat. Mater.* **17**, 778–782 (2018).
25. Tan, C. et al. Hard magnetic properties in nanoflake van der Waals Fe_3GeTe_2. *Nat. Commun.* **9**, 1554 (2018).
26. Liu, B. et al. Light-tunable ferromagnetism in atomically thin Fe_3GeTe_2 driven by femtosecond laser pulse. *Phys. Rev. Lett.* **125**, 267205 (2020).
27. Xie, T. et al. High-efficiency optical training of itinerant two-dimensional magnets. *Nat. Phys.* **21**, 1118–1124 (2025).
28. Xia, M. J. et al. Magnetic circular dichroism study of electronic transition in metal Fe_3GeTe_2. *J. Phys. Chem. C* **126**, 8152–8157 (2022).
29. Ho, C.-H., Peng, Y.-H. & Chen, Z.-Y. Microthermoreflectance characterization of the band-structure transformations observed during the magnetic-ordering transitions of multilayered 2D Fe_3GeTe_2 ferromagnetic metals. *Small Sci.* **5**, 2500293 (2025).
30. Roemer, R., Liu, C. & Zou, K. Robust ferromagnetism in wafer-scale monolayer and multilayer Fe_3GeTe_2. *NPJ 2D Mater. Appl.* **4**, 33 (2020).
31. Park, S. Y. et al. Controlling the magnetic anisotropy of the van der Waals ferromagnet Fe_3GeTe_2 through hole doping. *Nano Lett.* **20**, 95–100 (2020).
32. Cowburn, R. P., Ferré, J., Gray, S. J. & Bland, J. A. C. Domain-wall dynamics, pinning, and nucleation in ultrathin epitaxial Fe films. *Phys. Rev. B* **58**, 11507 (1998).
33. Jeudy, V. et al. Universal pinning energy barrier for driven domain walls in thin ferromagnetic films. *Phys. Rev. Lett.* **117**, 57201 (2016).
34. Franken, J. H., Hoeijmakers, M., Lavrijsen, R. & Swagten, H. J. M. Domain-wall pinning by local control of anisotropy in Pt/Co/Pt strips. *J. Phys. Condens. Matter* **24**, 024216 (2012).
35. Kläui, M. et al. Domain wall pinning in narrow ferromagnetic ring structures probed by magnetoresistance measurements. *Phys. Rev. Lett.* **90**, 097202 (2003).
36. Wu, N. et al. Photoinduced femtosecond spin-flip assisted by a single-mode linear phonon. *Sci. Adv.* **12**, eadv9616 (2026).
37. Zhang, K.-X., Park, G., Lee, Y., Kim, B. H. & Park, J.-G. Magneto-electric effect in van der Waals magnets. *NPJ Quantum Mater.* **10**, 6 (2025).

38. Zhang, K. et al. Gigantic current control of coercive field and magnetic memory based on nanometer-thin ferromagnetic van der Waals Fe_3GeTe_2. *Adv. Mater.* **33**, 1–8 (2021).
39. Zhang, K. et al. Highly efficient nonvolatile magnetization switching and multi-level states by current in single Van der Waals topological ferromagnet Fe_3GeTe_2. *Adv. Funct. Mater.* **31**, 2105992 (2021).
40. Huang, B. et al. Emergent phenomena and proximity effects in two-dimensional magnets and heterostructures. *Nat. Mater.* **19**, 1276–1289 (2020).
41. Zhao, Y. Y., Guo, Y., Zhou, S. & Zhao, J. XGT (X= Fe, Mn, Cr; G= Ge; T= Te): a family of two-dimensional ternary intrinsic magnetic materials. *Phys. Rev. Mater.* **6**, 044005 (2022).
42. Zhang, G. et al. Above-room-temperature strong intrinsic ferromagnetism in 2D van der Waals Fe_3GaTe_2 with large perpendicular magnetic anisotropy. *Nat. Commun.* **13**, 5067 (2022).
43. Deng, Y. et al. Gate-tunable room-temperature ferromagnetism in two-dimensional Fe_3GeTe_2. *Nature* **563**, 94–99 (2018).
44. Li, Q. et al. Patterning-induced ferromagnetism of Fe_3GeTe_2 van der Waals materials beyond room temperature. *Nano Lett.* **18**, 5974–5980 (2018).
45. Wang, H. et al. Above room-temperature ferromagnetism in wafer-scale two-dimensional van der Waals Fe_3GeTe_2 tailored by a topological insulator. *ACS Nano* **14**, 10045–10053 (2020).
46. Casola, F., van der Sar, T. & Yacoby, A. Probing condensed matter physics with magnetometry based on nitrogen-vacancy centres in diamond. *Nat. Rev. Mater.* **3**, 17088 (2018).
47. Wiesendanger, R. Spin mapping at the nanoscale and atomic scale. *Rev. Mod. Phys.* **81**, 1495–1550 (2009).
48. Bigot, J.-Y. & Vomir, M. Ultrafast magnetization dynamics of nanostructures. *Ann. Phys.* **525**, 2 (2013).
49. Li, J. X. et al. Electric control of valley polarization in monolayer WSe_2 using a van der Waals magnet. *Nat. Nanotechnol.* **17**, 721–728 (2022).
50. Yang, H. et al. Two-dimensional materials prospects for non-volatile spintronic memories. *Nature* **606**, 663–673 (2022).
51. Phan, M.-H. New research trends in electrically tunable 2D van der Waals magnetic materials. Preprint at https://doi.org/10.48550/arXiv.2303.05748 (2023).
52. Gish, J. T., Lebedev, D., Song, T. W., Sangwan, V. K. & Hersam, M. C. Van der Waals opto-spintronics. *Nat. Electron.* **7**, 336–347 (2024).
53. Meng, Y. et al. Photonic van der Waals integration from 2D materials to 3D nanomembranes. *Nat. Rev. Mater.* **8**, 498–517 (2023).
54. Liu, C. H., Zheng, J. J., Chen, Y. Y., Fryett, T. & Majumdar, A. Van der Waals materials integrated nanophotonic devices. *Opt. Mater. Express* **9**, 384–399 (2019).
55. Field, B., Schiffrin, A. & Medhekar, N. V. Correlation-induced magnetism in substrate-supported 2D metal-organic frameworks. *NPJ Comput. Mater.* **8**, 1–10 (2022).
56. Kresse, G. Ab initio molecular dynamics for liquid metals. *J. Non Cryst. Solids* **192**, 222–229 (1995).
57. Kresse, G. & Hafner, J. Ab initio molecular-dynamics simulation of the liquid-metal-amorphous-semiconductor transition in germanium. *Phys. Rev. B* **49**, 14251–14269 (1994).
58. Kresse, G. & Furthmuller, J. Efficiency of ab-initio total energy calculations for metals and semiconductors using a plane-wave basis set. *Comput. Mater. Sci.* **6**, 15–50 (1996).
59. Perdew, J. P., Burke, K. & Ernzerhof, M. Generalized gradient approximation made simple. *Phys. Rev. Lett.* **77**, 3865–3868 (1996).
60. Wang, X. D., Wang, D. S., Wu, R. Q. & Freeman, A. J. Validity of the force theorem for magnetocrystalline anisotropy. *J. Magn. Magn. Mater.* **159**, 337–341 (1996).
61. Grimme, S., Antony, J., Ehrlich, S. & Krieg, H. A consistent and accurate ab initio parametrization of density functional dispersion correction (DFT-D) for the 94 elements H-Pu. *J. Chem. Phys.* **132**, 154104 (2010).

Acknowledgements

We gratefully acknowledge technical support from NCHC and CINC-NTU, Taiwan.

Author contributions

C.-H.L. and H.-T.J. supervised the project. W.-Q.L. carried out material exfoliation and characterization, assisted by P.-L.C. and K.-H.P. C.-H.L. conceived the experiments. W.-Q.L. and J.-X.L. performed the measurements, assisted by C.-C.L., C.K., and C.-H.L. S.-H.H. and H.-T.J. provided theoretical support. All authors contributed to the discussion of the data in the manuscript and Supplementary Information.

Funding

This work was supported by the National Tsing Hua University (Grant No.: 114Q2708E1), the National Science and Technology Council (Grant Nos.: NSTC 114-2628-M-007-002, 113-2223-E-007-008-MY3, 112-2112-M-007-034-MY3), and Academia Sinica (Grant No.: AS-iMATE-113-12).

Competing interests

The authors declare no competing interests.

Additional information

Supplementary information The online version contains supplementary material available at https://doi.org/10.1038/s41467-026-77178-9.

Correspondence and requests for materials should be addressed to Horng-Tay Jeng or Chang-Hua Liu.

Peer review information *Nature Communications* thanks Xiaojun Wu and the other anonymous reviewer(s) for their contribution to the peer review of this work. A peer review file is available.

Reprints and permissions information is available at http://www.nature.com/reprints

Publisher's note Springer Nature remains neutral with regard to jurisdictional claims in published maps and institutional affiliations.

Open Access This article is licensed under a Creative Commons Attribution-NonCommercial-NoDerivatives 4.0 International License, which permits any non-commercial use, sharing, distribution and reproduction in any medium or format, as long as you give appropriate credit to the original author(s) and the source, provide a link to the Creative Commons licence, and indicate if you modified the licensed material. You do not have permission under this licence to share adapted material derived from this article or parts of it. The images or other third party material in this article are included in the article's Creative Commons licence, unless indicated otherwise in a credit line to the material. If material is not included in the article's Creative Commons licence and your intended use is not permitted by statutory regulation or exceeds the permitted use, you will need to obtain permission directly from the copyright holder. To view a copy of this licence, visit http://creativecommons.org/licenses/by-nc-nd/4.0/.

© The Author(s) 2026